A Thesis for the degree of Doctor of Philosophy

Unsteady Computational Simulation of Ice Protection Systems in Aircraft Icing using the Conjugate Heat Transfer Method

By

Esmaeil Esmaeilifar

Department of Mechanical and Aerospace Engineering

Graduate School

Gyeongsang National University

August 2023

Unsteady Computational Simulation of Ice Protection Systems in Aircraft Icing using the Conjugate Heat Transfer Method

A dissertation submitted to the Faculty of the Graduate School of the Gyeongsang National University

By

Esmaeil Esmaeilifar

In partial fulfilment of the requirements for the degree of Doctor of Philosophy

August 2023

Prof. Rho Shin Myong, Dissertation Supervisor

Approved by committees of the Graduate School of Gyeongsang National University in partial fulfilment of the requirements for the degree of Doctor of Philosophy

Dissertation Committee:

Prof. Dr. Hakjin Lee
Chairman

Prof. Dr. Jae Hyun Park

Dr. Ji Hong Kim

Prof. Dr. Prince Raj Lawrence Raj 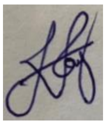

Prof. Dr. Rho Shin Myong
Supervisor

Date: 2023.07

Department of Mechanical and Aerospace Engineering
Graduate School
Gyeongsang National University

Acknowledgement

First, I would like to express my deepest gratitude to Professor Rho Shin Myong for his invaluable guidance, mentorship, and support throughout my academic journey. Professor Rho's profound knowledge, passion for research, and dedication to teaching have been instrumental in shaping my scientific understanding and research skills. His insightful feedback and constructive criticism have greatly enhanced my learning experience, and I am genuinely grateful for the opportunity to work under his mentorship.

Furthermore, I would like to express my appreciation to my colleagues in the ACML lab for their warm hospitality and support. I would also like to sincerely thank Bidesh Sengupta and Prince Lawrence Raj for their commitment to scientific discussions and valuable contributions to my research.

I am also grateful to Amin Rahmi and Omid Ejtehadi for their support and friendship. They have assisted me with research-related matters and provided a sense of camaraderie and support in navigating life in Korea. I am truly grateful for their presence and the lasting friendship we have built.

Esmaeil Esmaeilifar
July 14, 2023

Dedication

I dedicate this thesis to my beloved wife, Mina, whose unwavering love, support, and patience have been my constant source of strength throughout this journey.

I also want to thank my parents and sisters, who have always loved me unconditionally.

I also like to remember the memory of my dear friend Alireza Oliaye and our close friends Ali, Somaye, and Afagh, whose life was tragically cut short.

Table of Contents

Acknowledgement .... **iii**

Dedication .... **iv**

Table of Contents .... **v**

List of Figures .... **xi**

List of Tables .... **xvii**

Abstract .... **xviii**

Abstract in Korean .... **xxi**

Chapter 1. Introduction **1**

1.1 Overview of in-flight icing 1

1.1.1 Types of ice 2

1.1.2 Parameters affecting ice accretion 2

1.1.3 Atmospheric and flow conditions 2

1.1.4 Icing conditions 4

1.1.5 Surface conditions 6

1.1.6 Adverse effects of ice accretion 7

1.2 Overview of ice protection systems 8

1.2.1 Pneumatic boot de-icing IPS 9

1.2.2 Chemical systems 10

1.2.3 Bleed air IPS 12

1.2.4 Electrothermal IPS 13

1.3 Numerical modeling of electrothermal ice protection systems 15

1.4 Literature review 16

1.4.1 Review of de-icing solvers 16

1.4.2 Review of anti-icing solvers 20

1.5 Objectives and outline 24

Chapter 2. Compressible Navier-Stokes Air Solver 26

2.1 Turbulence modeling with the transition 26

2.2 Discretization of convective fluxes 29

2.3 Discretization of viscous fluxes 30

2.4 Temporal discretization 32

2.5 Dual time-stepping 33

2.6 Boundary conditions 34

2.6.1 Wall boundary condition 34

2.6.2 Far-field boundary condition 35

2.6.3 Symmetry boundary condition 36

Chapter 3. Eulerian-based Droplet Solver 38

3.1 Shallow water-type droplet equations 39

3.2 Spatial discretization of SWDE 39

3.3 Temporal discretization of SWDE 42

3.4 Permeable wall boundary condition 42

3.5 Supercooled large droplet modelling 43
3.5.1 SLD effects 44
Chapter 4. Droplet Wall Interaction 46
4.1 Surface wettability 46
4.2 Droplet impact dynamics 49
4.3 Droplet impact outcomes 50
4.4 Semi-empirical models 52
4.4.1 Trujillo model 54
4.4.2 Honsek and Habashi model 57
4.4.3 Bai and Gosman model 57
4.4.4 Wright and Potapczuk model 58
4.4.5 Trontin and Villedieu model 58
4.5 Proposed model for supercooled large droplets 60
4.6 Proposed model for superhydrophobic surfaces 61
4.7 Numerical Implementation 64
4.7.1 Modification of collection efficiency 64
4.7.2 Modification of boundary conditions 65
4.7.3 Modification of governing equations 65
4.8 Validation of the SLD model 66
Chapter 5. PDE-based Ice Solver 69
5.1 Thin film dynamics 69

5.1.1 Continuity equation 70

5.1.2 Momentum equation.. 71

5.2 System of equations 74

5.3 Compatibility relations.. 76

5.4 Finite volume formulation.. 77

5.5 Roe scheme 79

5.6 Modified ice solver 81

5.6.1 Temperature-based ice solver.. 81

5.6.2 Heat flux-based ice solver 87

Chapter 6. Multilayer Heat Conduction Solver 89

6.1 Governing equations and numerical implementation 89

6.2 Boundary conditions 91

6.2.1 Neumann boundary condition 91

6.2.2 Convective boundary condition.. 91

6.2.3 The interface of composite layers.. 92

6.3 Verification study.. 93

6.3.1 Case 1 (1D Slab, Dirichlet Boundary Condition).. 94

6.3.2 Case 2 (1D Slab, Mixed Boundary Condition) 96

6.3.3 Case 3 (1D slab, Neumann Boundary Condition) 97

6.3.4 Case 4 (1D Composite Slab) 99

6.3.5 Case 5 (2D Plate).. 101

Chapter 7. Conjugate Heat Transfer 103

7.1 Weak coupling approaches 103

7.2 Interface boundary conditions 106

7.2.1 Dirichlet-Neumann boundary conditions 106

7.2.2 Robin boundary conditions 107

7.3 Coupling ice and conduction solvers 108

7.3.1 Temperature-based coupling 109

7.3.2 Flux-based coupling 110

7.4 Coupling air and conduction solvers 112

7.5 Full coupling of air, ice, and conduction solvers 113

Chapter 8. Electrothermal De-Icing IPS 116

8.1 Geometry and conditions 116

8.2 Independence of results to the numerical parameters 119

8.3 Validation of electrothermal de-icing solver 121

8.4 Analysis of the electrothermal de-icing process 127

Chapter 9. Electrothermal Anti-Icing IPS 136

9.1 Dry air anti-icing simulations 137

9.2 Wet anti-icing simulations 142

9.2.1 Anti-icing simulation of case 22A 143

9.2.2 Anti-icing simulation of case 22B 147

9.2.3 Anti-icing simulation of case 67A 151

9.2.4 Anti-icing simulation of case 67B 156
9.3 Heat load analysis 160
9.3.1 Running wet mode 162
9.3.2 Fully evaporative mode 166
9.3.3 Novel adjustable operating condition 168
Chapter 10. Superhydrophobic Surfaces in Aircraft Icing 174
10.1 Droplet wall interaction on a superhydrophobic surface 175
10.2 Slip effect on runback water film 176
10.3 Ice accretion on a superhydrophobic surface 178
Chapter 11. Conclusion and Future Works 182
11.1 Concluding remarks 182
11.2 Future works 184
Bibliography 186

List of Figures

Figure 1-1 Effect of temperature on ice accretion. 3

Figure 1-2 Effect of flow velocity on ice accretion. 3

Figure 1-3 Effect of angle of attack on ice accretion. 4

Figure 1-4 Effect of droplet diameter on ice accretion. 5

Figure 1-5 Ice accretion on (a) aircraft engine inlet, (b) aircraft wing, (c) Pitot tube, and (d) rotorcraft engine intake (adopted from [29]). 8

Figure 1-6 Function of pneumatic boot de-icing IPS..10

Figure 1-7 Ethylene glycol-based liquid dripping out from tiny holes on the wing to prevent ice formation using the TKS ice protection system. 11

Figure 1-8 (a) Bleed air IPS for engine inlet, (b) schematic of the bleed air system, (c) streamlines of hot air in a piccolo tube. 13

Figure 1-9 Electrothermal wing IPS for Boeing 787. 13

Figure 1-10 Examples of electrothermal IPS applications: (a) Engine intake of the KAI KUH-1 Surion helicopter (left) and icing test results of a helicopter engine air intake (right); (b) IPS on an airplane wing (left) and schematic of an electro-thermal IPS with heater pads (right); (c) rotor blade of the KAI KUH-1 Surion helicopter (left) and schematic of a rotor blade de-icing system (right). 15

Figure 1-11 Schematic of anti-icing and de-icing process in aircraft icing. 15

Figure 2-1 Skin friction coefficient over a flat plate with natural laminar to turbulent transition. 29

Figure 2-2 Cell-Centered scheme: Linear reconstruction. 30

Figure 2-3 Stencil for the gradient computation for the cell-centered scheme. 31

Figure 2-4 Wall boundary condition for the cell-centered scheme...35

Figure 2-5 Far-field boundary condition for (a) inflow and (b) outflow. 35

Figure 3-1 The HLLC approximate Riemann scheme for SWEs. 40

Figure 3-2 Permeable wall boundary condition. 43

Figure 4-1 Contact Angle of a droplet on a perfectly smooth surface (Adopted from [17]). ..47

Figure 4-2 Wenzel (left) and Cassie–Baxter (right) states (Adopted from [16]). 48

Figure 4-3 Illustration of advancing and receding contact angle for a droplet on an inclined surface (Adopted from [17]). 48

Figure 4-4 Schematic of droplet impact dynamics (Adopted from [89]). 50

Figure 4-5 Summary of droplet impact outcomes (adopted from [83]). 51

Figure 4-6 Schematic of droplet wall interaction outcomes. 52

Figure 4-7 Schematic of droplet wall interaction. 55

Figure 4-8 Effect of advancing contact angle on (a) critical Cossali parameter and (b) critical incidence angle (right) for MVD=20μm. 63

Figure 4-9 Collection efficiency results for (a) MVD=52 μm, (a) MVD=111 μm, (a) MVD=154 μm, (a) MVD=236 μm, ...68

Figure 5-1 Schematic of thin water film on the surface with partial slip. 73

Figure 5-2 Mass (left) and energy (right) balance for runback water film. 75

Figure 5-3 Flow chart of PDE-based ice accretion solver. 79

Figure 5-4 The algorithm of the temperature-based ice solver. 83

Figure 5-5 Schematic of ice, runback water, and melted water control volumes. 84

Figure 6-1 Information mapping from mult-zone to single-zone grid. 89

Figure 6-2 Stencil for the temperature gradient computation. 90

Figure 6-3 Cells adjacent to the interface between layers with different thermal properties. .93

Figure 6-4 Initial and boundary conditions for verification test case 1. 95

Figure 6-5 Error norms (left) and temperature profile along the slab (right) for verification test case (1). 96

Figure 6-6 Initial and boundary condition for verification test case 2....................................96

Figure 6-7 Error norms (left) and temperature change versus time (right) for verification case (1)..97

Figure 6-8 Initial and boundary condition for verification test case 3....................................98

Figure 6-9 Error norms (left) and temperature profile along the slab (right) for case (3). 98

Figure 6-10 Initial and boundary conditions for verification test case 4. 99

Figure 6-11 Error norms (left) and temperature profile along the slab (right) for verification test case (3). 101

Figure 6-12 Initial and boundary condition for verification test case 5.................................101

Figure 6-13 Error norms (left) and temperature profile along the y direction of plate (right) for verification test case (5)..102

Figure 7-1 (a) Loosely coupled and (b) tightly coupled approaches for the temperature-based coupling of ice (I) and conduction (C) solvers. 105

Figure 7-2 Schematic of interface boundary condition of type F_QS_T (left) and F_TS_Q (right).107

Figure 7-3 Schematic of the interface boundary condition of type F_hS_T (left) and F_hS_Q (right). 108

Figure 7-4 Change in enthalpy of ice/water near the critical temperature.............................110

Figure 7-5 Tightly coupled approach for the flux-based coupling of ice (I) and conduction (C) solvers. 111

Figure 7-6 Flowchart of loosely coupled approach for air (A) and conduction (C) solvers..112

Figure 7-7 Comparison of decoupled (left) and loosely coupled (right) solvers flowcharts. 113

Figure 7-8 Flowchart of loosely coupled approach for air (A) and ice/conduction (IC) solvers. 115

Figure 8-1 Composite layering and arrangement of heaters in the leading edge..................117

Figure 8-2 Computational domain consisting of solid and fluid grids. 117

Figure 8-3 Heater cycle sequence for the electrothermal de-icing process. 118

Figure 8-4 Temperature change over time (a) for different CHT coupling time steps and (b) for various artificial phase change temperature ranges for case 1. 120

Figure 8-5 Temperature change over time at (a) heater A, (b) heater B, and (c) heater D for case 1 (left) and case 2 (right). 122

Figure 8-6 Temperature change over time at (a) heater A, (b) heater B, and (c) heater D for case 1 (left) and case 2 (right). 126

Figure 8-7 Distribution of surface temperature at different times (105s, 110s, 115s, 120s) for case 1. 127

Figure 8-8 Profiles of (a) Temperature; (b) de-icing heat load; (c) ice accretion rate; (d) water film thickness; (e) ice mass; and (f) ice melting rate at different times (1.4s to 4.9s) for case 1. 130

Figure 8-9 Profiles of (a) Temperature; (b) de-icing heat load; (c) ice mass; and (d) water film thickness at different times (10s to 100s) for case 1. 131

Figure 8-10 Ice shape, water film, and temperature contours at different times for case 1. (For visualization purposes, ice height and water film were scaled up two times and 100 times, respectively). 135

Figure 9-1 Schematic of different anti-icing regimes based on water film extent, impingement limits, and protection limits. 136

Figure 9-2 Illustration of Δt_{CHT}, air solver physical time step, and pseudo iterations. 138

Figure 9-3 Temperature distribution (a) and temperature variation of heater B over time (b) for different Δt_{CHT} and $N_p/\Delta t_A$. 139

Figure 9-4 Comparison between the current loosely coupled and Bu's tightly coupled approaches for temperature and h_c profiles of dry anti-icing case 22B. 141

Figure 9-5 Comparison of h_c distribution for case 22 with isothermal wall temperature of 280K. 141
Figure 9-6 Distribution of (a) runback water mass flow rate, (b) surface temperature, (c) convective heat transfer coefficient and (d) global heat transfer coefficient for anti-icing test case 22A. 145
Figure 9-7 Temperature contours and ice ridge formation obtained by (a) decoupled and (b) loosely coupled solvers for case 22A. 146
Figure 9-8 Distribution of (a) runback water mass flow rate, (b) surface temperature, (c) convective heat transfer coefficient, and (d) global heat transfer coefficient for anti-icing test case 22B. 149
Figure 9-9 Temperature contours and ice ridge formation obtained by (a) decoupled and (b) loosely coupled solvers for case 22A. 150
Figure 9-10 Distribution of (a) runback water mass flow rate, (b) surface temperature, (c) convective heat transfer coefficient, and (d) global heat transfer coefficient for anti-icing test case 67A. 153
Figure 9-11 Comparison of (a) convective heat transfer coefficient and (b) surface temperature between fully turbulent and transitional SA turbulence model for anti-icing test case 67A. 154
Figure 9-12 Temperature contours and ice ridge formation obtained by (a) decoupled and (b) loosely coupled solvers for case 67A. 155
Figure 9-13 Distribution of (a) runback water mass flow rate, (b) surface temperature, (c) convective heat transfer coefficient and (d) global heat transfer coefficient for anti-icing test case 67B. 158
Figure 9-14 Temperature contours and ice ridge formation obtained by (a) decoupled and (b) loosely coupled solvers for case 67B. 159
Figure 9-15 Flowchart for prediction of heat load based on icing and operating conditions 161

Figure 9-16 Heat flux density required for running wet mode at different target wall temperatures. 163

Figure 9-17 Total heat required for running wet mode at different target wall temperatures. 164

Figure 9-18 (a) Runback ice and (b) water film thickness at different target wall temperatures for running wet mode, case 22. 165

Figure 9-19 (a) Wall temerpature distribution and (b) Heat flux density required for fully evaporative mode, case 22. 167

Figure 9-20 Water film thickness at different Δt_{evap} for case 22 169

Figure 9-21 Comparison of runback ice at different Δt_{evap} for case 22. 170

Figure 9-22 (a) Full and (b) truncated heat flux density required for different Δt_{evap}, case 22. 171

Figure 9-23 Total heat required for running wet mode at different Δt_{evap}, case 22. 172

Figure 9-24 Comparison of heat power density for various anti-icing modes, case 22 173

Figure 10-1 Effect of advancing contact angle on collection efficiency. 176

Figure 10-2 Mean water film velocity at different times and slip lengths. 177

Figure 10-3 Water film thickness at different times and slip lengths. 177

Figure 10-4 Comparison of water film thickness (left) and mean water film velocity at different slip lengths. 179

Figure 10-5 Comparison of ice shape for different advancing contact angles. 181

List of Tables

Table 1-1 Comparison of different de-icing solvers available in the literature. 16

Table 1-2 Comparison of different anti-icing solvers available in the literature. 21

Table 6-1 Boundary conditions of verification cases. 94

Table 6-2 Error norms for case 1. 95

Table 6-3 Error norms for case 2. 97

Table 6-4 Error norms for case 3. 98

Table 6-5 Error norms for case 4. 100

Table 6-6 Error norms for case 5. 102

Table 8-1 Material properties of the composite layers. 118

Table 8-2 Heater powers and icing conditions for the validation cases. 119

Table 9-1 Heater powers and icing conditions for anti-icing validation cases. 137

Abstract

Unsteady Computational Simulation of Ice Protection Systems in Aircraft Icing using the Conjugate Heat Transfer Method

Esmaeil Esmaeilifar

Department of Mechanical and Aerospace Engineering

Graduate School, Gyeongsang National University

Supervised by Prof. Rho Shin Myong

In-flight icing occurs when an aircraft or rotorcraft fly through icing clouds, and supercooled water droplets impact the surface of the flying vehicle. Ice accumulation on the wing, engine inlet, cockpit windows, and pitot tube of aircraft can degrade aerodynamic performance and handling quality. Designing reliable and efficient ice protection systems is essential to mitigate the adverse effect of ice accretion and ensure a safe flight. Electrothermal ice protection systems have become popular due to their compatibility with more electric aircraft trends and composite structures. Moreover, it can be utilized as a hybrid ice protection system in conjunction with emerging superhydrophobic coating, which can save a significant amount of energy.

Employing experimental tests to design ice protection systems is limited due to the high cost, lack of facilities, and scalability issues. Developing accurate and reliable computational solvers can significantly decrease costs and speed up the design and certification processes. In this study, a unified framework was developed to simulate electrothermal ice protection systems in aircraft icing. The electrothermal ice protection system framework comprises several solvers, including a compressible Navier-Stokes-Fourier airflow solver, a Eulerian

droplet impingement solver, an unsteady ice accretion/melting solver, and a heat conduction solver. These solvers are formulated using partial differential equations and implemented within a unified finite volume framework. This approach allows for the use of a single grid system, eliminating the need for additional grid generation specifically for the ice layer.

Ice and conduction solvers were tightly coupled using the conjugate heat transfer method, where the runback water and ice domain were linked to the multilayer solid domain by exchanging thermal boundary conditions at the interface. The electrothermal de-icing solver was validated using experimental data from electrothermal de-icing tests conducted in the NASA Lewis Icing Research Tunnel. The de-icing process was also studied by analyzing the runback water film, ice accretion/melting, and temperature distribution on the surface.

Moreover, the air solver was loosely coupled with ice/conduction solvers to update the airflow based on the transient wall temperature distribution calculated in the ice/conduction solvers. Interestingly, the anti-icing results obtained by the loosely coupled solver were also compared with the decoupled solver and experimental data for different anti-icing regimes. Results obtained by coupled solver are in better agreement with experimental data compared to the decoupled solver, especially in the leading edge's aft region. Finally, a novel framework was developed to evaluate the required heat load at running wet, evaporative, and fully evaporative anti-icing modes.

In order to simulate ice accretion on superhydrophobic surfaces, two modifications were applied to the droplet and ice solvers. First, the semi-empirical supercooled large droplet model, which was developed to consider the effects of droplet/wall interaction, was modified to consider the wettability effects on collection efficiency. Second, the lubrication theory equations were revisited to modify the shallow water icing model considering the partial slip boundary conditions. Results show that the droplet deposition rate decreases by increasing the surface contact angle. Moreover, increasing the contact angle can result in different ice-type formations at the same atmospheric and icing conditions.